Progress In Electromagnetics Research C, Vol. 172, 434–447, 2026

PIER C

(Received 2 June 2026, Accepted 24 July 2026, Scheduled 21 August 2026)

Research on Model-Free Direct Speed Control of PMSM Based on Second-Order Ultra-Local Model

Yanan Zhou, Lin Li, Xinxin Zheng*, Tong Liu, and Yao He

College of Automotive and Traffic Engineering, Hefei University of Technology, Hefei 230009, China

ABSTRACT: This paper proposes a model-free direct speed control (MFDC) method based on a second-order ultra-local model to address the speed loop bandwidth issue and difficulty of further improving dynamic response performance in the speed control of a traditional cascaded permanent magnet synchronous motor drive system. The speed control method based on an accurate mathematical model has poor robustness to unknown disturbances, such as parameter uncertainty and inverter nonlinearity. This method eliminates the double closed-loop cascade structure of the traditional speed outer loop and q-axis current inner loop. By establishing a second-order ultra-local model of the surface-mounted permanent magnet synchronous motor (SMPMSM) drive system considering parameter uncertainty and inverter nonlinearity, the mechanical speed of the motor was directly related to the inverter's output voltage, and a model-free direct speed controller integrating speed control and torque current control functions was designed. Simultaneously, a model-free current controller based on the first-order current ultra-local model is used to realize the independent adjustment of the d-axis stator current. In addition, a virtual q-axis current ultra-local model torque limitation method for direct speed control is proposed to realize an effective constraint of electromagnetic torque without a cascade structure. Experimental results demonstrate that the proposed method provides enhanced load-disturbance rejection, particularly under medium- and high-speed conditions. At 500 r/min, load-step speed fluctuation is reduced from 3.6152% to 2.0638%, and recovery time is shortened from 0.0288 s to 0.0080 s. Under the rated-speed step condition, the speed overshoot is reduced from 2.8028% to 2.2136%.

1. INTRODUCTION

Driven by intensifying global energy crisis and environmental concerns, the electric vehicle (EV) industry has ushered in unprecedented development opportunities in recent years. As the core propulsion source of EVs, the performance of the motor drive system directly dictates the vehicle's dynamic response, energy efficiency, and ride comfort [1, 2]. Permanent magnet synchronous motors (PMSMs) are widely utilized in critical automotive subsystems, such as traction drives, steer-by-wire systems, and brake-by-wire systems, owing to their high power density, superior efficiency, and compact structure [3]. Particularly in the power-coupling scenarios of plug-in hybrid electric vehicles (PHEVs), precise and synchronous speed control between the engine and motor is a prerequisite for ensuring safe and stable vehicle operation. Consequently, research on high-performance speed-control technologies has significant engineering value [4].

In conventional PMSM drive control architectures, the cascaded proportional-integral (PI) control framework based on field-oriented control (FOC) has long been the dominant paradigm owing to its structural simplicity and ease of implementation [5]. However, this cascaded configuration exhibits inherent limitations: the bandwidth of the outer speed loop is significantly lower than that of the inner current loop, creating a bottleneck that restricts the system's dynamic response [6]. Furthermore, PI controller parameter tuning heavily relies on empirical engineering experience, making it challenging to maintain optimal control performance across diverse operating conditions [7]. More importantly, practical PMSM drive systems are inevitably subjected to various perturbations, including parameter uncertainties, inverter nonlinearities, sudden load-torque disturbances, and unmodelled dynamics. These disturbances can severely degrade the control quality of speed regulation methods that rely on precise mathematical models [8, 9].

To overcome performance bottlenecks associated with cascaded control, direct speed control methodologies have been explored. By integrating the outer speed loop and inner q-axis current loop, direct speed control establishes a direct mapping between motor speed and inverter output voltage [10]. Model predictive control (MPC) has emerged as a promising technical path for implementing direct speed control, due to its native capability to handle multi-input multi-output systems and physical constraints [11, 12]. In [13], a sliding manifold incorporating speed and torque errors was introduced into the MPC cost function to accelerate the speed error convergence. A dual-cost-function design was proposed in [14] to optimize dynamic and steady-state performance sequentially, achieving comprehensive improvement through a two-stage voltage vector selection process. To mitigate the large current ripples caused by step changes in the output voltage, reference [15] introduced a finite control set of voltage vectors characterized by adjustable amplitudes and movable origins. To reduce the tuning burden associated with model predictive torque control, a weighting-

* Corresponding author: Xinxin Zheng (xinxin.zheng@hfut.edu.cn).

factor-free strategy combined with a composite sliding-mode disturbance observer was developed in [16]. This method improves robustness against parameter mismatch and eliminates the need to tune weighting coefficients. Nevertheless, it remains a model-predictive torque-control approach whose implementation relies on torque- and flux-related prediction variables. Despite these advancements, MPC-based direct speed control still faces several challenges. First, tuning weighting factors in multi-objective cost functions remains heuristic and labor-intensive. Second, controller performance depends on an accurate system model, meaning that parameter mismatch can degrade prediction accuracy or even cause instability [17]. Third, although some methods consolidate cascaded loops at the controller level, they still retain cascaded characteristics within their underlying prediction models [18].

To mitigate the reliance of model-based methods on precise physical parameters, model-free control (MFC) techniques have been developed. The core concept of MFC is to estimate unknown disturbances and system uncertainties online using historical input-output data via algebraic parameter identification, thereby constructing an online-updated ultra-local model for controller design [19]. In [20], an MFC was combined with model predictive direct speed control, employing a variable-weight cost function with two current-error terms to balance dynamic and steady-state performances under varying conditions. An adaptive direct speed control scheme using integral dynamic variables was proposed in [21], where the adaptive coefficients were adjusted via gradient descent to enhance robustness. However, while these methods nominally achieve direct speed control, their prediction models fundamentally mirror the cascaded structure of the physical system, failing to bypass separate modeling frameworks of the speed and current loops.

Active disturbance rejection control (ADRC) and extended state observer (ESO)-based methods are also closely related to the disturbance-estimation principle adopted in this study. ADRC treats internal uncertainties and external disturbances as a generalized disturbance, which is reconstructed online by an ESO and compensated through the control input [22]. ESO-based PMSM controllers have therefore been developed to suppress effects of load-torque variations, parameter uncertainties, inverter nonlinearities, and unmodeled dynamics [23]. Although ADRC/ESO and ultra-local-model-based MFC both rely on lumped-disturbance estimation and compensation, their estimation mechanisms are different. ESO-based methods augment disturbance as an additional state and estimate it using a dynamic observer, whereas the present MFC method directly estimates the lumped term from finite-window input-output data via algebraic parameter identification [24]. Moreover, most existing ESO-based PMSM controllers introduce disturbance compensation into a conventional speed or current loop [25]. In contrast, the proposed method establishes a second-order speed ultra-local model from mechanical speed to q-axis reference voltage, removes explicit q-axis current loop from the speed-control channel, and realizes torque limiting via a virtual q-axis current ultra-local model [26].

To address limitations of first-order approximations, ref. [27] introduced a second-order ultra-local model tailored for second-order systems, along with an intelligent proportional-integral-derivative (i-PID) controller. Applying a second-order ultra-local model to PMSM direct speed control has the potential to eliminate cascaded characteristics at the predictive model level, thereby enabling a highly dynamic, noncascaded direct speed control framework. Nevertheless, literature addressing second-order ultra-local model-based direct speed control for PMSMs remains scarce, and further theoretical analysis and experimental validation are required.

This study's main research contents and innovations are summarized as follows: A second-order dynamic mathematical model from speed to q-axis stator voltage for a surface-mounted permanent magnet synchronous motor (SMPMSM) is established. By integrating the speed loop and q-axis current loop, a second-order speed ultra-local model was constructed and eliminated the bandwidth limitation of the cascaded structure. The online estimation of lumped disturbances is realized via the algebraic parameter identification method, which completely eliminates the need for an accurate mathematical model of the motor. A torque limiting method based on a virtual q-axis current ultra-local model is proposed. Fast disturbance estimation is achieved using the sampling data of adjacent control cycles. A q-axis current prediction model was constructed, and the q-axis reference voltage clamping interval under rated torque constraints was derived. Torque safety constraints for direct speed control were realized under a low computational load. An experimental bench for the SMPMSM drive system was built based on the dSPACE rapid control prototyping platform. Comparative experiments under multiple operating conditions verified the advantages of the proposed method in terms of dynamic response and robustness, which provides experimental support for the engineering application of this method in electric-vehicle electric-drive systems.

The comparison indicates that the novelty of the proposed method lies in the combined realization of second-order speed-to-voltage ultra-local modeling, non-cascaded direct speed regulation, and virtual q-axis current-based torque limiting. The proposed approach does not simply add a disturbance estimator to a conventional speed or current loop; instead, it restructures the speed-control channel at the model level.

This paper's main contributions are summarized as follows:

(1) A second-order speed ultra-local model is established to directly relate the SMPMSM's mechanical speed to the q-axis reference voltage. Unlike conventional cascaded MFC schemes, the proposed model incorporates the speed-loop and q-axis current-loop dynamics into a unified speed-to-voltage formulation, thereby removing the explicit q-axis current loop from the speed-control channel and the associated cascaded bandwidth separation.

(2) A model-free direct speed controller is developed based on the finite-window algebraic estimation of lumped disturbance. The controller directly generates the q-axis reference voltage and compensates online for the aggregated effects of parameter uncertainties, inverter nonlinearities, load-torque variations, and unmodeled dynamics, without requiring a complete and accurately identified motor model.

(3) A torque-limiting strategy based on a virtual q-axis current ultra-local model is proposed for the non-cascaded control architecture. By using adjacent-cycle current and voltage samples to estimate the virtual lumped term and predict the q-axis current, the method derives the allowable q-axis voltage interval under the rated-torque constraint. Consequently, bidirectional torque limitation is achieved without introducing an additional load-torque observer or reconstructing a cascaded q-axis current-control loop.

(4) Comparative experiments over multiple speed-step and load-step operating conditions are conducted on a dSPACE-based SMPMSM test platform. The results clarify both the performance advantages of the proposed method under medium- and high-speed load disturbances and its remaining limitations under low-speed speed-step conditions.

2. MATHEMATICAL MODEL OF SMPMSM

2.1. Mathematical Model Considering Multi-Source Disturbances

In practical drive systems, SMPMSMs are inevitably subjected to multi-source disturbances with varying characteristics. These include electrical parameter variations caused by temperature increases in the stator windings, mechanical parameter perturbations (such as variations in the moment of inertia and viscous damping coefficient), stator voltage distortion induced by inverter nonlinearities (e.g., dead-time effects and power-device conduction voltage drops), unmodeled dynamics, and measurement noise. These disturbances degrade the performance of controllers designed under ideal model assumptions, which can potentially compromise system stability.

To accurately characterize the system's dynamic behavior under these nonideal factors, the mathematical model of the SMPMSM drive system is modified as follows:

$$\frac{d\omega_m}{dt} = \frac{T_e}{J} - \frac{T_L}{J} - \frac{B}{J}\omega_m + \frac{1}{J}f_\omega \tag{1}$$

$$\frac{di_d}{dt} = \frac{1}{L_s}u_d^* - \frac{R_s}{L_s}i_d + n_p\omega_m i_q - \frac{1}{L_s}(V_{d,par} + V_{d,dead}) \tag{2}$$

$$\frac{di_q}{dt} = \frac{1}{L_s}u_q^* - \frac{R_s}{L_s}i_q - n_p\omega_m\left(i_d + \frac{\varphi_f}{L_s}\right) - \frac{1}{L_s}(V_{q,par} + V_{q,dead}) \tag{3}$$

where f_ω denotes the lumped disturbance term caused by mechanical parameter uncertainties and unknown disturbances; $V_{d,par}$ and $V_{q,par}$ are the disturbance voltages induced by electrical parameter uncertainties in the dq-axis; $V_{d,dead}$ and $V_{q,dead}$ are the disturbance voltages caused by inverter nonlinear effects in the dq-axis, which contain harmonic components related to rotor synchronous rotational frequency. Notably, because actual dq-axis stator voltages are typically difficult to measure in practical setups, the stator voltages in the equation are replaced by their reference values u_d^* and u_q^*. Consequently, any voltage discrepancies induced by inverter nonlinearities are naturally absorbed into the lumped system disturbances. In (1), J denotes the total equivalent moment of inertia referred to the motor shaft rather than only the rotor inertia of the tested SMPMSM. For the experimental drive system, it includes the rotor inertia of the tested motor and the equivalent inertias of the dynamometer, coupling, adapter shaft, and other rotating components.

2.2. Second-Order Speed Ultra-Local Model

The overall derivation flow of the second-order speed ultra-local model is schematically illustrated in Figure 1. To eliminate bandwidth limitation inherent in a cascade structure, this study directly develops a second-order dynamic mathematical model relating motor mechanical speed ω_m to q-axis stator reference voltage u_q^*. By integrating this formulation into the speed control loop, a second-order ultra-local speed model was established.

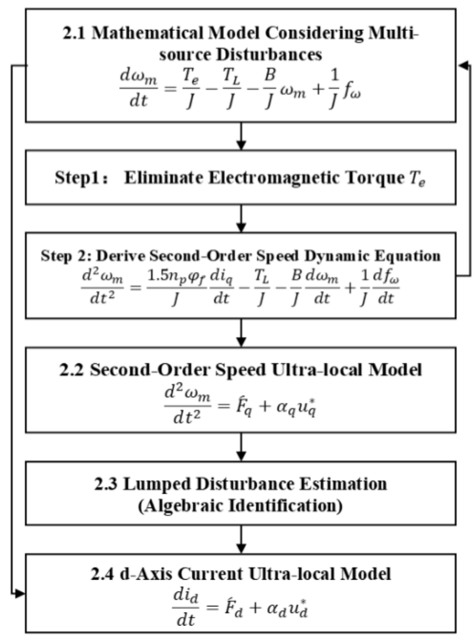

FIGURE 1. Derivation process of second-order speed ultra-local model.

Substituting the electromagnetic torque equation into the mechanical motion equation in (1) and eliminating the electromagnetic torque T_e yields a relationship between speed and q-axis current:

$$\frac{d\omega_m}{dt} = \frac{1.5n_p\varphi_f i_q}{J} - \frac{T_L}{J} - \frac{B}{J}\omega_m + \frac{1}{J}f_\omega \tag{4}$$

Differentiating both sides of (4) with respect to time yields the second-order differential expression of the rotor speed:

$$\frac{d^2\omega_m}{dt^2} = \frac{1.5n_p\varphi_f}{J}\frac{di_q}{dt} - \frac{1}{J}\frac{dT_L}{dt} - \frac{B}{J}\frac{d\omega_m}{dt} + \frac{1}{J}\frac{df_\omega}{dt} \tag{5}$$

Substituting (3) into (5) yields the second-order speed mathematical model of the SMPMSM drive system, which explicitly accounts for parameter uncertainties, inverter nonlinearities, and external disturbances as follows:

$$\frac{d^2\omega_m}{dt^2} = \frac{1.5n_p\varphi_f}{J}\left(\begin{array}{c} \frac{1}{L_s}u_q^* - \frac{R_s}{L_s}i_q - n_p\omega_m\left(i_d + \frac{\varphi_f}{L_s}\right) \\ -\frac{1}{L_s}(V_{q,par} + V_{q,dead}) \end{array}\right)$$

$$-\frac{1}{J}\frac{dT_L}{dt}-\frac{B}{J}\frac{d\omega_m}{dt}+\frac{1}{J}\frac{df_\omega}{dt} \tag{6}$$

By choosing mechanical speed ω_m as the system output and q-axis stator reference voltage u_q^* as the control input, (6) can be rewritten in a standard second-order ultra-local model format:

$$\frac{d^2\omega_m}{dt^2}=F_q+\alpha_q u_q^* \tag{7}$$

where α_q represents the scaling factor of the second-order speed ultra-local model, selected as $1.5n_p\varphi_f/(JL_s)$ according to nominal motor parameters to ensure dynamic matching between the input and output.

It should be emphasized that "model-free" does not mean that no nominal information is used to initialize the controller. Instead, it means that the online control law does not require a complete and accurately identified physical model of the PMSM drive system. The coefficient α_q provides an input-output scaling relationship, while the effects of parameter mismatch and unmodeled dynamics are incorporated into the lumped term F_q.

To illustrate this property, let the actual input gain of speed-to-voltage dynamics be b_q. The system can be expressed as:

$$\frac{d^2\omega_m}{dt^2}=f_q+b_q u_q^* \tag{8}$$

For a selected scaling coefficient α_q, the above equation is equivalently rewritten as:

$$\frac{d^2\omega_m}{dt^2}=[f_q+(b_q-\alpha_q)u_q^*]+\alpha_q u_q^* \tag{9}$$

Therefore, the mismatch between the actual input gain and selected scaling coefficient is included in the lumped term F_q and estimated online. Nevertheless, α_q affects the effective feedback gain and disturbance-estimation magnitude. An excessively small value may amplify voltage-command and measurement-noise fluctuations, whereas an excessively large value may reduce the speed-error convergence rate. Consequently, α_q should have the same sign as the actual input gain and should be selected within a reasonable magnitude range.

F_q expresses the lumped disturbance of the second-order speed ultra-local model, whose expression is given by:

$$\begin{aligned}F_q=&\left(\frac{1.5n_p\varphi_f}{JL_s}-\alpha_q\right)u_q^*+\frac{1.5n_p\varphi_f}{J}\\&\left(-\frac{R_s}{L_s}i_q-n_p\omega_m\left(i_d+\frac{\varphi_f}{L_s}\right)-\frac{V_{q,par}+V_{q,dead}}{L_s}\right)\\&-\frac{B}{J}\frac{d\omega_m}{dt}-\frac{1}{J}\frac{dT_L}{dt}+\frac{1}{J}\frac{df_\omega}{dt}\end{aligned} \tag{10}$$

As can be seen from the expression for F_q, this lumped disturbance term aggregates all internal parameter variations, inverter nonlinearities, viscous damping, and load torque disturbances. Consequently, there is no need to design individual observers for each disturbance. The online estimation and feedforward compensation of F_q via algebraic parameter identification are sufficient to achieve comprehensive disturbance rejection, thereby simplifying controller design and eliminating dependency on detailed nominal motor models.

2.3. Lumped Disturbance Term Estimation

An algebraic parameter identification method was employed to estimate lumped disturbance F_q online. By applying the Laplace transform and differential operations to the second-order ultra-local model, this method eliminates the influence of the system's initial states. Simultaneously, integral operations were introduced to suppress high-frequency measurement and sampling noise, yielding a real-time estimator expressed solely in terms of historical input and output data.

Assuming that the lumped disturbance F_q is constant within one control period, taking the Laplace transform of (7) yields the frequency-domain expression:

$$s^2\Omega_m(s)=\frac{F_q}{s}+\alpha_q U_q^*(s)+s\omega_m(0)+\dot{\omega}_m(0) \tag{11}$$

where $\Omega_m(s)$ and $U_q^*(s)$ denote Laplace transforms of the mechanical speed $\omega_m(t)$ and q-axis voltage reference $u_q^*(t)$, respectively. The terms $\omega_m(0)$ and $\dot{\omega}_m(0)$ represent the initial states of the speed and their first derivatives, respectively.

To eliminate the influence of initial conditions $\omega_m(0)$ and $\dot{\omega}_m(0)$, differentiating the above expression with respect to s twice consecutively yields:

$$\frac{2F_q}{s^3}=s^2\frac{d^2\omega_m}{ds^2}+4s\frac{d\omega_m}{ds}+2\Omega_m(s)-\alpha_q\frac{d^2U_q^*}{ds^2} \tag{12}$$

Since positive powers of s correspond to time-domain differentiation (which is highly sensitive to noise) and negative powers correspond to integration, both sides of (12) are multiplied by s^{-3} to eliminate all positive powers of s. Applying the inverse Laplace transform then yields the continuous time-domain estimator for F_q, denoted as $\hat{F}_q$:

$$\begin{aligned}\hat{F}_q\;=\;&\frac{60}{T_{Fq}^5}\int_0^{T_{Fq}}\left(T_{Fq}^2+6\sigma^2-6T_{Fq}\sigma\right)\omega_m(\sigma)d\sigma\\&-\frac{30\alpha}{T_{Fq}^5}\int_0^{T_{Fq}}(T_{Fq}-\sigma)^2\sigma^2u_q^*(\sigma)d\sigma\end{aligned} \tag{13}$$

where T_{Fq} is the time window length for sliding estimation, which is equal to n_qT_s; T_s is the control period; and σ is the integration time variable. The sliding-window length n_q, or equivalently the time-window duration $T_{Fq}=n_qT_s$, determines the trade-off between noise attenuation and disturbance-tracking speed. A larger n_q increases the integral smoothing effect of the algebraic estimator and suppresses sampled-speed noise more effectively. However, it also increases the estimator's effective memory and delays the estimation of rapidly varying disturbances. In contrast, a smaller n_q improves the estimator's transient tracking capability but increases fluctuations in $\hat{F}_q$ and the resulting q-axis voltage command. Consequently, n_q should be selected by jointly considering measurement noise, disturbance variation rate, voltage-command smoothness, and closed-loop transient performance.

Considering the discrete sampling characteristics of digital control systems, the composite trapezoidal rule is applied to numerically solve the above definite integral, yielding a discrete estimation formula suitable for real-time computation:

$$\begin{aligned}\hat{F}_q \;=\; & \frac{30}{n_q^5 T^2}\sum_{i=0}^{n_q-1}\left[\begin{array}{c}\left(n_q^2+6i^2-6n_q i\right)\omega_m(i)+\\ \left(n_q^2+6(i+1)^2-6n_q(i+1)\right)\\ \omega_m(i+1)\end{array}\right]\\ & -\frac{15\alpha}{n_q^5}\sum_{i=0}^{n_q-1}\left[\begin{array}{c}(n_q-i)^2 i^2 u_q^*(i)+\\ (n_q-(i+1))^2(i+1)^2 u_q^*(i+1)\end{array}\right] \qquad (14)\end{aligned}$$

where i denotes the index of the sampling points in the time window; $\omega_m(i)$ is the motor speed at the i-th sampling instant; and $u_q^*(i)$ is the q-axis reference voltage at the same instant. Using Equation (14), the lumped disturbance $\hat{F}_q$ can be estimated online using only the input-output data from the current and preceding n_q control cycles, conforming to the core design principles of model-free control.

Substituting $\hat{F}_q$ for F_q in (7) yields the following second-order speed ultra-local model of the SMPMSM drive system, which is independent of the accurate mathematical model and accounts for multiple disturbances including parameter uncertainties:

$$\frac{d^2\omega_m}{dt^2}=\hat{F}_q+\alpha_q u_q^* \qquad (15)$$

2.4. d-Axis Current Ultra-Local Model

For d-axis current control, this study adopts the modeling framework based on the first-order ultra-local model to establish the d-axis current ultra-local model as follows:

$$\frac{di_d}{dt}=\hat{F}_d+\alpha_d u_d^* \qquad (16)$$

where the scaling factor α_d is selected as $\alpha_d = 1/L_s$ according to the nominal value of the stator inductance. The lumped disturbance $\hat{F}_d$ encapsulates all known and unknown disturbances, including the stator resistance voltage drop, back-EMF coupling term, parameter uncertainties, and inverter nonlinearities. Based on the first-order algebraic parameter identification method, the discrete estimation formula for $\hat{F}_d$ is given by:

$$\begin{aligned}\hat{F}_d \;=\; & -\frac{3}{n_d^3 T_s}\sum_{i=0}^{n_d-1}\left[(n_d-2i)i_d(i)+\alpha_d i(n_d-i)u_d^*(i)\right.\\ & +(n_d-2(i+1))i_d(i+1)\\ & \left.+\alpha_d(i+1)(n_d-(i+1))u_d^*(i+1)\right] \qquad (17)\end{aligned}$$

Consequently, the second-order speed ultra-local model and first-order d-axis current ultra-local model of the SMPMSM drive system were established, providing a robust, noncascaded foundation for controller design.

3. DIRECT SPEED CONTROLLER DESIGN

3.1. Model-Free Direct Speed Controller

Based on the established second-order speed ultra-local model, a speed-tracking error was introduced for dynamic closed-loop regulation, and a model-free direct speed controller was designed. This controller directly generates the q-axis stator reference voltage from the reference speed, actual speed, and estimated lumped disturbance. Consequently, it completely bypasses the conventional cascaded configuration that couples an outer speed loop with an inner q-axis current loop.

To achieve steady-state error-free tracking of the step reference speed, integral action was introduced into the controller structure, resulting in the following form of the model-free direct speed controller, whose block diagram is shown in Fig. 2:

$$u_q^*=\frac{-\hat{F}_q+\dfrac{d^2\omega_m^*}{dt^2}+K_{pq}(\omega_m^*-\omega_m)+K_{iq}\int(\omega_m^*-\omega_m)}{\alpha_q} \qquad (18)$$

where K_{pq} is the scaling gain factor, and K_{iq} is the integral gain factor. In the practical discrete-time implementation, the second-order derivative term of the reference speed in (18) is omitted. The reference-speed command used in experiments is piecewise constant, and direct numerical differentiation at the step transition of the piecewise constant reference speed may generate a large impulse and increase sensitivity to sampled-signal noise.

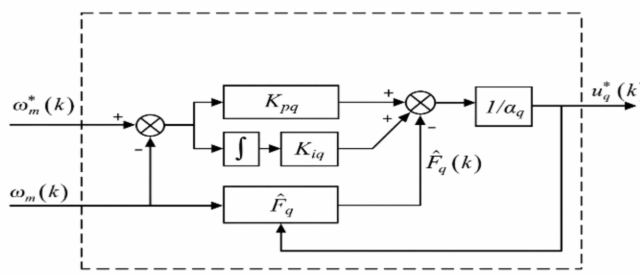

FIGURE 2. Practical implementation block diagram of the model-free direct speed controller.

The designed direct speed controller counteracts the effects of all lumped disturbances in the system through the feedforward compensation of $\hat{F}_q$ and achieves high-precision speed tracking via PI closed-loop regulation. Meanwhile, it directly establishes the control mapping from the reference speed to the q-axis reference voltage, completely eliminating the bandwidth limitations between the speed loop and the q-axis current loop in the conventional cascade structure, which can significantly improve the dynamic response performance of the speed.

3.2. d-Axis Current Controller

For control of d-axis stator current, a model-free current controller based on a first-order current ultra-local model is adopted. Because the surface-mounted permanent magnet synchronous motor (SMPMSM) adopts the $i_d^* = 0$ maximum torque per ampere (MTPA) control strategy, the primary

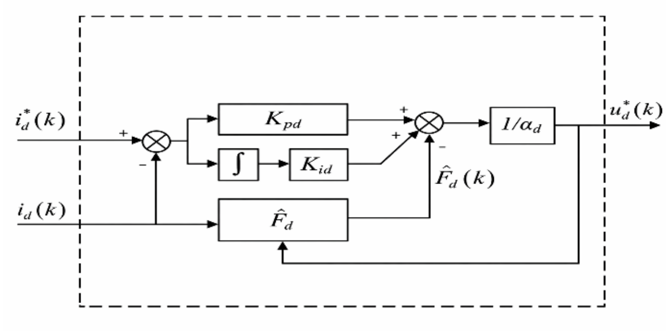

FIGURE 3. Practical implementation block diagram of the model-free d-axis current controller.

objective of the d-axis current controller is to maintain the d-axis current near zero and avoid unnecessary direct-axis armature reaction. The resulting model-free d-axis current controller is given below, and its block diagram is shown in Fig. 3:

$$u_d^* = \frac{-\hat{F}_d + \frac{di_d^*}{dt} + K_{pd}(i_d^* - i_d) + K_{id}\int(i_d^* - i_d)}{\alpha_d} \tag{19}$$

Similarly, the derivative term $\frac{di_d^*}{dt}$ in Eq. (19) is omitted in the practical implementation. Since the d-axis reference current is fixed at $i_d^* = 0$ throughout the experiments, its derivative is zero.

4. TORQUE LIMITING STRATEGY

In conventional cascaded speed control systems, the outer speed loop outputs either the q-axis reference current or reference electromagnetic torque. Consequently, physical constraints on the electromagnetic torque and stator current can be easily implemented by applying saturation limits to the speed controller's output. Under the direct speed control framework, however, the speed loop and q-axis current loop are integrated. The controller directly synthesizes the q-axis stator reference voltage without generating intermediate variables, such as reference torque or reference current. Therefore, a novel torque-limiting method designed for noncascaded structures is necessary to prevent the motor from triggering overcurrent protection or suffering permanent magnet demagnetization owing to transient current overshoots during high-torque operations, such as startup and acceleration. To address this challenge, this section proposes a torque-limiting strategy based on a virtual q-axis current ultra-local model. By avoiding complex load-torque observers, this approach enforces rigorous torque constraints using only sampled data from adjacent control periods, minimizing computational overhead while the remaining is entirely independent of the nominal motor parameters.

4.1. Virtual q-Axis Current Ultra-Local Model

The core concept of this strategy is based on the assumption that a q-axis current ultra-local model exists at a virtual level. The state information of the q-axis current was estimated using sampled data from adjacent control periods. Then, the allowable range of the q-axis reference voltage that satisfies the rated torque constraint is calculated using deadbeat predictive control principles.

Based on the first-order ultra-local model framework, virtual q-axis current dynamics can be expressed as:

$$\frac{di_q}{dt} = F_{qu} + \alpha_{qu} u_q^* \tag{20}$$

where α_{qu} is the scaling factor of the virtual q-axis current ultra-local model, which is selected as $\alpha_{qu} = 1/L_s$, and F_{qu} is the lumped disturbance term of the q-axis current loop, which aggregates all internal and external disturbances related to q-axis current dynamics, including stator resistance voltage drop, back EMF, parameter uncertainties, and inverter nonlinearities.

Discretizing (20) using the forward Euler method yields one-step-ahead predictive model of the q-axis stator current:

$$i_q(k+1) = i_q(k) + T_s(F_{qu}(k) + \alpha_{qu} u_q^*(k-1)) \tag{21}$$

where $i_q(k+1)$ is the predicted q-axis stator current at the $(k+1)$-th control period, and $u_q^*(k-1)$ is the q-axis stator reference voltage at the $(k-1)$-th control period.

To reduce the computational burden, F_{qu} is no longer estimated using the integral method of algebraic parameter identification but is calculated by adjacent-period difference approximation based on sampled data from two consecutive control periods. According to (21), the estimated disturbance $\hat{F}_{qu}(k)$ at the current control period k is calculated as:

$$\hat{F}_{qu}(k) = \frac{i_q(k) - i_q(k-1)}{T_s} - \alpha_{qu} u_q^*(k-1) \tag{22}$$

where $i_q(k-1)$ is the q-axis stator current at the $(k-1)$-th control period, and $u_q^*(k-1)$ is the q-axis stator reference voltage at the $(k-1)$-th control period.

Assuming that F_{qu} remains constant during consecutive control periods, we have:

$$\hat{F}_{qu}(k-1) = \hat{F}_{qu}(k) = \hat{F}_{qu}(k+1) \tag{23}$$

Furthermore, the forward Euler method is applied to predict the q-axis current at the $(k+2)$-th control period as follows:

$$i_q(k+2) = i_q(k+1) + T_s(\hat{F}_{qu}(k+1) + \alpha_{qu} u_q^*(k)) \tag{24}$$

where $i_q(k+2)$ is the predicted q-axis stator current at the $(k+2)$-th control period.

4.2. q-Axis Voltage Clipping under Torque Constraints

From the electromagnetic torque equation, the motor's rated electromagnetic torque T_{en} corresponds to the rated q-axis current i_{qN} as follows:

$$i_{qN} = \frac{2T_{en}}{3n_p\varphi_f} \tag{25}$$

To ensure that the motor's electromagnetic torque does not exceed its physical limit, the q-axis current must be constrained to satisfy $|i_q| \leq |i_{qN}|$. Based on deadbeat predictive control, by setting $i_q(k+2)$ in (24) equal to i_{qN} and $-i_{qN}$ respectively, and combining (21)–(23), the upper and lower bounds of the q-axis reference voltage ($u^*_{q,\max}$ and $u^*_{q,\min}$) can be derived as follows:

$$u^*_{q\max} = \frac{\dfrac{\dfrac{T_{en}}{1.5n_p\varphi_f} - i_q(k+1)}{T} - \hat{F}_{qu}(k+1)}{\alpha_{qu}} \tag{26}$$

$$u^*_{q\min} = \frac{\dfrac{-\dfrac{T_{en}}{1.5n_p\varphi_f} - i_q(k+1)}{T} - \hat{F}_{qu}(k+1)}{\alpha_{qu}} \tag{27}$$

Therefore, the allowable range of the q-axis reference voltage satisfying rated torque constraint is $[u^*_{q,\min}, u^*_{q,\max}]$. The q-axis reference voltage generated by the direct speed controller is subjected to limiting processing, and the limiting rule is as follows:

$$u^*_q(k) = \begin{cases} u^*_q(k), & u^*_{q,\min}(k) \le u^*_q(k) \le u^*_{q,\max}(k) \\ u^*_{q,\max}(k), & u^*_q(k) \ge u^*_{q,\max}(k) \\ u^*_{q,\min}(k), & u^*_q(k) \le u^*_{q,\min}(k) \end{cases} \tag{28}$$

Using the above limiting rule, safe constraints on electromagnetic torque and q-axis current can be realized in direct speed control. This method has the following significant advantages: First, it is independent of the accurate mathematical model of the motor. Mismatches in the stator resistance, inductance, and permanent magnet flux linkage are implicitly included in the difference estimation of F_{qu}, which has little impact on torque limiting accuracy. Second, it can simultaneously realize bidirectional limiting of positive and negative torques, considering torque protection requirements under both motoring and braking conditions.

The overall architecture of the proposed model-free direct speed control system for the SMPMSM drive is presented in Figure 4.

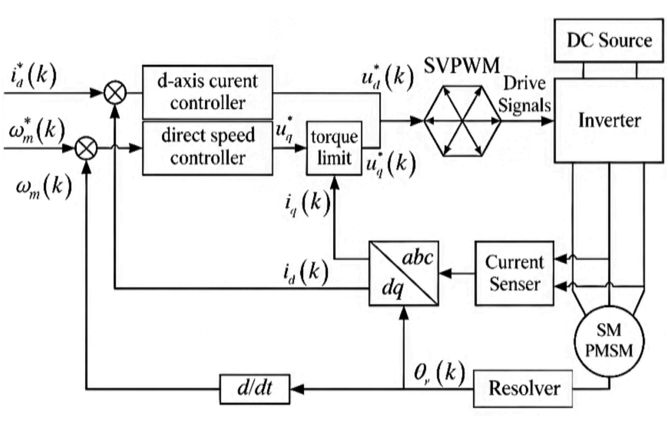

FIGURE 4. Structure block diagram of model-free direct speed control for SMPMSM drive system.

5. EXPERIMENTAL RESULTS

To verify the effectiveness of the proposed model-free direct speed control (MFDC) method based on the second-order ultra-local model, an experimental test bench for the SMPMSM drive system was built based on the dSPACE rapid control prototyping platform. Comparative experiments under multiple operating conditions were conducted using the conventional cascaded model-free speed control (MFC) method, and the speed step response performance and load-disturbance rejection performance of the two methods were tested.

5.1. Experimental Platform and Parameter Configuration

Experiments were conducted on the experimental test bench shown in Fig. 5. The test bench mainly consisted of the tested SMPMSM, a load dynamometer, a three-phase two-level voltage-source inverter, a dSPACE DS5202 rapid control prototyping controller, a DC power supply, current sensors, and a resolver. The SMPMSM's nominal parameters are listed in Table 1. The dynamometer is a 2.2 kW induction asynchronous motor, which is controlled by an ABB ACS800 frequency converter to operate in the torque mode to provide load torque for the tested motor. The inverter uses MOSFETs as switching devices, and the dead time is set to 2.5 µs. The DC bus voltage was set to 48 V. Three-phase stator currents were sampled in real time using LEM LA25-P Hall current sensors, and the rotor position and speed were sampled in real time using a resolver. The control algorithm was modeled in MATLAB/Simulink, downloaded to the DS5202 controller for execution via the dSPACE real-time code generation tool, and real-time control and data acquisition were realized through the ControlDesk host computer.

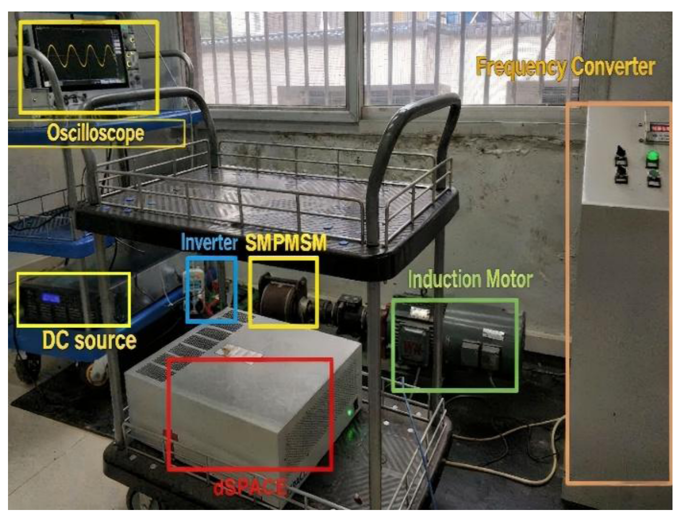

FIGURE 5. SMPMSM experimental test bench.

Nominal parameters of the tested SMPMSM are listed in Table 1. It should be noted that the rotor moment of inertia listed for the motor is $J = 0.01015$ kg·m^2, whereas the mechanical dynamics of the experimental system are determined by the total equivalent inertia moment referred to the motor shaft. In addition to the rotor inertia of the tested SMPMSM,

TABLE 1. Comparison of PMSM speed-control approaches.

Method	Dependence on motor model	Direct q-axis voltage generation	Disturbance estimation	Torque-constraint implementation
MFC	Low	No	Separate ultra-local estimation in individual loops	Current-reference saturation
MPDSC	Generally medium or high	Yes	Model-based prediction or additional observer	Cost function or explicit constraints
ADRC/ESO-based PMSM control	Reduced	Depends on implementation	Dynamic extended-state observer	Usually current or voltage saturation
Proposed MFDC	Reduced	Yes	Second-order finite-window algebraic estimator	Virtual q-axis current model and voltage clipping

the total equivalent inertia includes those of the dynamometer, coupling, adapter shaft, and other rotating components. For the experimental platform, the total equivalent inertia moment is $J_{\text{tot}} = 0.04242$ kg·m^2. Therefore, the scaling factor of the second-order speed ultra-local model is calculated as $\alpha_q = (1.5 \times 12 \times 0.027)/(0.04242 \times 0.001) \approx 11456.86$. The calculated value was adopted in the experimental implementation of the proposed MFDC method. This distinction between the motor rotor inertia and the total equivalent shaft-system inertia is necessary because the speed controller regulates the dynamics of the complete mechanically coupled experimental system rather than those of the unloaded motor rotor alone.

During comparative experiments, for the conventional MFC method, the current-loop control period was 100 µs, and the speed-loop control period was 1 ms; for the proposed MFDC method, the control period was 100 µs. Both methods adopted the same SVPWM algorithm to generate the inverter driving signals, and the d-axis reference current was set to $i_d^* = 0$ for both methods. The key controller parameters were set as follows: for the conventional MFC method: $\alpha_\omega = 98.52$, $\alpha_d = \alpha_q = 1000$, and the time window length was $n = 10$. For the proposed MFDC method: $\alpha_q = 11456.86$, $\alpha_d = \alpha_{qu} = 1000$, the time window length of the second-order ultra-local model was $n_q = 80$, and the time window length of the d-axis current ultra-local model was $n_d = 10$. Speed controller parameters are $K_{pq} = 45824$, $K_{iq} = 0.35$; d-axis current controller parameters are $K_{pd} = 9000$, $K_{id} = 0$. A rapid control prototyping model of the model-free speed control for the SMPMSM drive system, which includes the dSPACE low-level drivers, was built in MATLAB/Simulink for code generation for the dSPACE/DS5202 rapid prototyping controller.

For the second-order lumped-disturbance estimator, the control period is $T_s = 100$ µs, and the sliding-window length is selected as $n_q = 80$. Therefore, the corresponding estimation-window duration is $T_{Fq} = n_q T_s = 8$ ms. This window duration is considerably shorter than the measured mechanical speed-response time scale, which is approximately 0.16–0.33 s in MFDC speed-step experiments. The 8-ms window corresponds to approximately 2.4%–5.0% of the measured recovery time. A shorter window improves disturbance-tracking speed but produces larger fluctuations in the estimated lumped term and q-axis voltage command, whereas a longer window provides stronger noise attenuation but causes a slower disturbance-estimation response. Based on compromise among estimation smoothness, transient response, and voltage-command fluctuations, $n_q = 80$ was selected for experimental implementation.

To evaluate the repeatability of experimental results, each operating condition was tested independently five times using the same controller parameters, initial conditions, reference commands, and load-torque settings. The performance indices reported in Tables 2 and 3 are the arithmetic mean values obtained from the five repeated trials. These results indicate that the experimental measurements exhibit good repeatability.

TABLE 2. Nominal parameters of the SMPMSM.

Parameter name	Parameter value
Rated torque	13 N·m
Rated speed	500 r/min
Rated current	19 A_{rms}
Pole pairs	12
Stator resistance	0.0957 Ω
Stator inductance	1 mH
Permanent magnet flux linkage	0.027 Wb
Motor rotational inertia	0.01015 kg·m^2
Total moment of inertia	0.04242 kg·m^2

5.2. Speed Step Response Experimental Analysis

To verify the speed dynamic response performance of the proposed method, no-load startup experiments with step reference speed commands are conducted. With the motor at a standstill with zero speed, the reference speed was stepped to 100, 300 and 500 r/min at $t = 1$ s, corresponding to three typical operating conditions: low, medium and rated speeds. In the experiments, the response waveforms of the mechanical speed ω_m, d-axis current i_d, q-axis current i_q, and estimated lumped disturbance $\hat{F}_q$ were recorded in real time. It should be noted that the estimated F_q of the proposed method is the sum of known and unknown disturbance components from both the speed and q-axis current loops in the conventional cascade-structure speed control. It has a different scale from the estimated F_q of the conventional model-free speed control for the SMPMSM drive

TABLE 3. Comparison of dynamic response performance of two speed control methods under speed-step condition.

Control Method	Operating Speed (r/min)	Overshoot (%)	Recovery Time (s)
MFC	100	10.9601	0.1693
	200	5.9291	0.2013
	300	3.8827	0.1383
	400	3.2740	0.2199
	500	2.8028	0.2128
MFDC	100	12.0615	0.3342
	200	10.5004	0.1741
	300	4.8576	0.2175
	400	3.5961	0.1596
	500	2.2136	0.1949

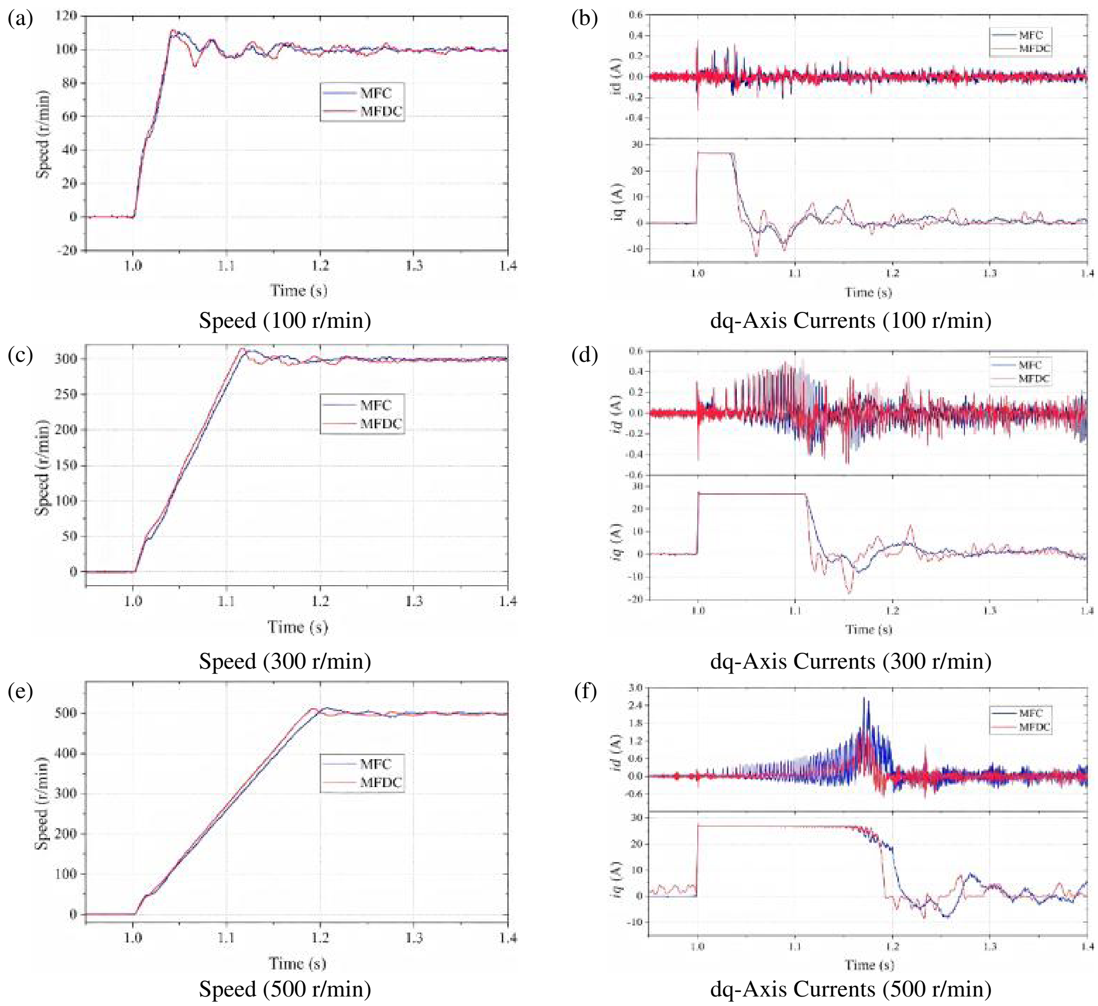

FIGURE 6. Experimental results of speed step response.

system; therefore, a direct comparison is not feasible. Therefore, only the waveform of the estimated F_q using the proposed method is provided. The experimental results are shown in Fig. 6.

Figures 6(a) and 6(b) show the mechanical speed and dq-axis stator currents under a 100 r/min speed step response. It can be seen from the figure that for the conventional MFC method, the speed rise time is 0.12 s, the overshoot is 10.96%, and the recovery time is 0.1693 s; for the proposed MFDC method, the speed rise time is 0.15 s, the overshoot is 12.06%, and the recovery time is 0.3342 s. Under low-speed operation, both methods can realize the speed's zero-static-error tracking. The over-

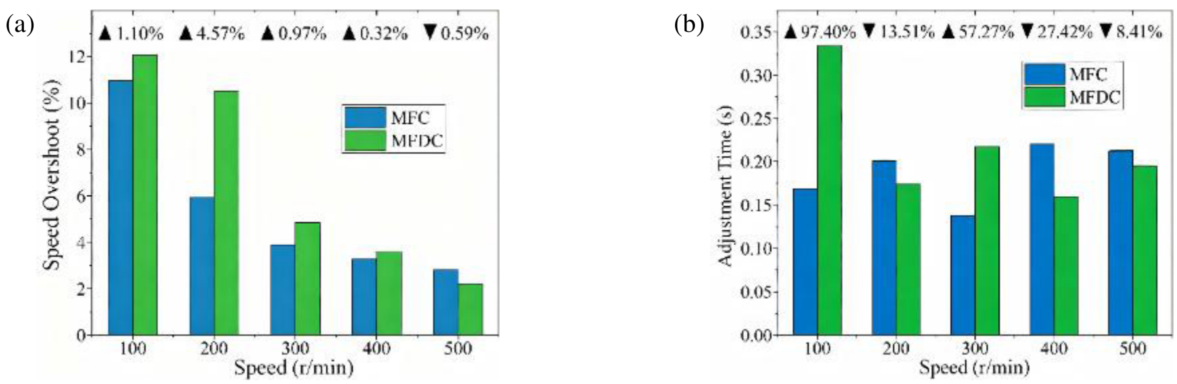

Speed Overshoot

Recovery Time

FIGURE 7. Comparison of dynamic response performance of two control methods under speed-step condition. (a) Speed overshoot and (b) recovery time.

shoot of the MFDC method is slightly larger than that of the MFC method. This behavior is attributed to the lower signal-to-noise ratio of the speed derivative obtained from the resolver at low speeds. Because the MFDC is a single-loop second-order controller with high gains designed to regulate speed directly, the high-frequency measurement noise propagates more prominently into the voltage command, requiring a longer duration to settle than the heavily damped cascaded MFC.

Figures 6(c) and 6(d) show the mechanical speed and dq-axis stator currents under a 300 r/min speed step response. For the conventional MFC, the speed overshoot is 3.88% and the recovery time is 0.1383 s, while the MFDC exhibits an overshoot of 4.86% and a recovery time of 0.2175 s. As the operating speed increases, the signal-to-noise ratio (SNR) of the speed measurement improves, reducing the gap between the two methods. Both schemes maintain steady-state speed and current ripples within acceptable limits.

Figures 6(e) and 6(f) show the mechanical speed and dq-axis stator currents under a 500 r/min speed step response. Here, the conventional MFC yields an overshoot of 2.80% and a recovery time of 0.2128 s. In contrast, the proposed MFDC achieves a lower overshoot of 2.21% (a 21.1% relative reduction) and a shorter recovery time of 0.1949 s. Near the rated operating limit, the proposed MFDC demonstrates superior transient behavior, characterized by reduced overshoot, faster stabilization, and lower current ripples.

The comparison of dynamic response performance metrics between the two methods under different speed-step operating conditions is shown in Fig. 7.

As shown in Fig. 7 and Table 2, relative percentage changes are calculated with respect to corresponding results of the conventional MFC method. The proposed MFDC does not provide uniform improvement over the entire speed range. At 100, 200, 300, and 400 r/min, the MFDC exhibits larger speed overshoots than the conventional MFC. In particular, at 100 r/min, the overshoot increases from 10.9601% to 12.0615%, and the recovery time increases from 0.1693 s to 0.3342 s. This indicates that the proposed second-order direct speed controller is more sensitive to sampled-speed fluctuations and disturbance-estimation delay under low-speed operating conditions.

At 200 and 400 r/min, although the MFDC produces slightly larger overshoots, its recovery times are reduced from 0.2013 s to 0.1741 s and from 0.2199 s to 0.1596 s, respectively. At 300 r/min, both the overshoot and recovery time of the MFDC are larger than those of the conventional MFC. Therefore, speed-step results indicate that the proposed method does not consistently outperform the conventional MFC under all low- and medium-speed operating conditions.

The clearest improvement is observed at the rated speed of 500 r/min. The MFDC reduces the speed overshoot from 2.8028% to 2.2136%, corresponding to a relative reduction of approximately 21.0%. Meanwhile, the recovery time decreases from 0.2128 s to 0.1949 s, corresponding to a relative reduction of approximately 8.4%. These results demonstrate that the proposed method provides improved speed-step transient performance near the rated operating point. However, further improvement in low-speed and disturbance estimations are required to extend this advantage to the entire operating-speed range.

The dynamic response performance data of the two methods under all speed-step operating conditions are listed in Table 2.

5.3. Experimental Analysis of Load Disturbance Rejection

To verify the robustness of the proposed method against load disturbances, comparative experiments were conducted under load-step operating conditions. In the experiments, the motor first operated stably under the given reference speed with a load torque of 10 N·m, which was applied by the dynamometer. After the system reached a steady state, the load was suddenly reduced to 0 N·m at $t = 9$ s, and the transient response process of speed, current, and estimated lumped disturbance was observed. The experiments were conducted under three speed operating conditions of 100, 300, and 500 r/min. The experimental results are shown in Fig. 8.

Figures 8(a) and 8(b) show the mechanical speed and dq-axis stator currents under a 100 r/min speed step response. Following the load rejection, the conventional MFC exhibits a peak speed rise of 21.58 r/min (a 21.58% transient speed fluctuation) with a recovery time of 0.1399 s. The proposed MFDC reduces peak speed deviation to 14.45 r/min (a 14.45% speed fluctua-

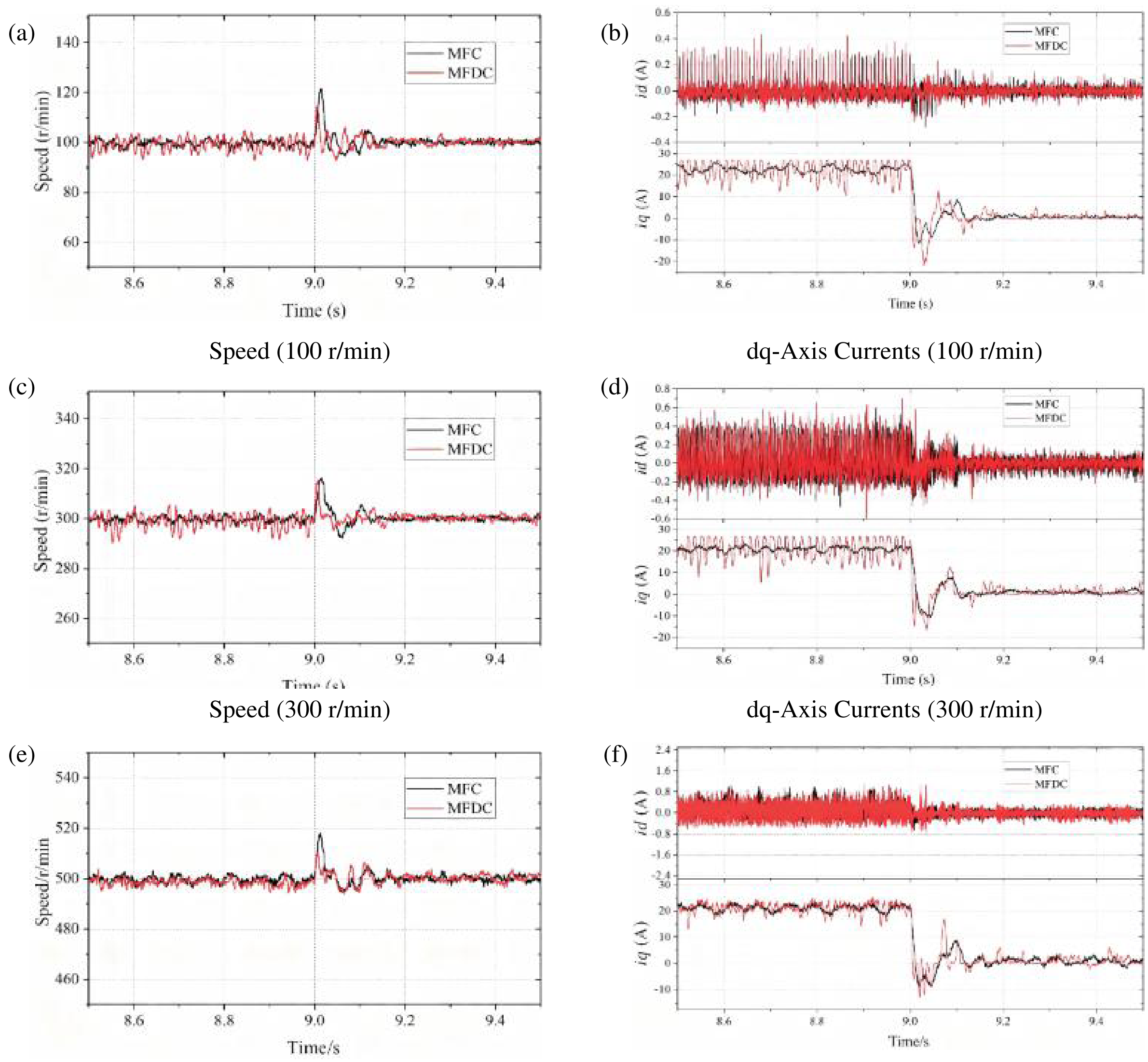

Speed (100 r/min) dq-Axis Currents (100 r/min)

Speed (300 r/min) dq-Axis Currents (300 r/min)

Speed (500 r/min) dq-Axis Currents (500 r/min)

FIGURE 8. Experimental results of load-step response.

tion), which is 33.0% lower than that of the MFC and stabilizes within 0.1693 s. This demonstrates stronger disturbance-rejection capability at low operating speeds.

Figures 8(c) and 8(d) show the mechanical speed and dq-axis stator currents under 300 r/min speed step response. Under the conventional MFC, the speed fluctuation is 5.41% with a recovery time of 0.0639 s. The proposed MFDC reduces the speed deviation to 5.04% and shortens the recovery time to 0.011 s — an 82.8% reduction compared to the MFC. At medium speeds, the MFDC significantly accelerates the recovery to the nominal speed.

Figures 8(e) and 8(f) show the mechanical speed and dq-axis stator currents under a 500 r/min rated speed step response. For conventional MFC, the speed deviation is 3.62% with a recovery time of 0.0288 s. The proposed MFDC restricts the speed rise to 2.06% (a 42.9% reduction) and recovers in 0.008 s (a 72.2% reduction). At rated speed, the proposed MFDC minimizes transient speed deviations and restores steady-state operation rapidly, demonstrating robust disturbance rejection.

The comparison of dynamic response performance metrics between the two methods under load-step operating conditions with different speeds is shown in Fig. 9.

As shown in Fig. 9 and Table 3, the proposed MFDC generally provides stronger load-disturbance rejection than the conventional MFC. The relative percentage changes shown in Fig. 9 are calculated using the conventional MFC results as the reference. At 100 r/min, the MFDC reduces transient speed fluctuation from 21.5772% to 14.4455%, corresponding to a relative reduction of approximately 33.1%. However, the recovery time increases from 0.1399 s to 0.1693 s, representing a deterioration of approximately 21.0%. Therefore, at this low-speed operating point, the proposed method effectively suppresses the peak speed deviation but requires a longer time to restore steady-state operation.

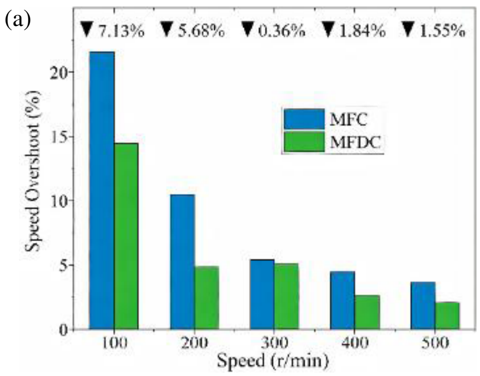

Speed Overshoot

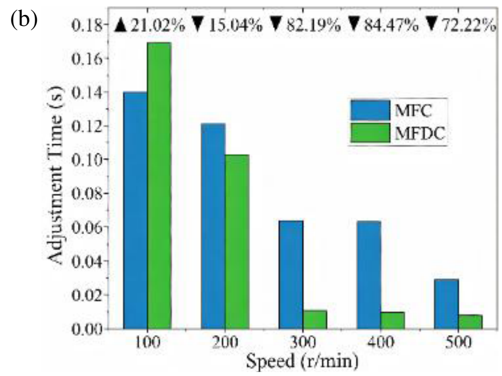

Recovery Time

FIGURE 9. Comparison of dynamic response performance under load step disturbance. (a) Speed overshoot and (b) recovery time.

TABLE 4. Comparison of dynamic response performance of two speed control methods under load-step condition.

Control Method	Operating Speed (r/min)	Overshoot (%)	Recovery Time (s)
MFC	100	21.5772	0.1399
	200	10.5050	0.1210
	300	5.4077	0.0639
	400	4.4642	0.0631
	500	3.6152	0.0288
MFDC	100	14.4455	0.1693
	200	4.8287	0.1028
	300	5.0432	0.0110
	400	2.6249	0.0098
	500	2.0638	0.0080

At 200 r/min, the speed fluctuation is reduced from 10.5050% to 4.8287%, corresponding to a relative reduction of approximately 54.0%, while the recovery time is shortened from 0.1210 s to 0.1028 s, corresponding to a reduction of approximately 15.0%. At 300 r/min, the improvement in the peak speed fluctuation is relatively limited, decreasing from 5.4077% to 5.0432%, or approximately 6.7%. Nevertheless, the recovery time is substantially reduced from 0.0639 s to 0.0110 s, corresponding to an improvement of approximately 82.8%.

More significant improvements are obtained at 400 and 500 r/min. At 400 r/min, the MFDC reduces the speed fluctuation by approximately 41.2% and the recovery time by approximately 84.5%. At 500 r/min, the speed fluctuation decreases from 3.6152% to 2.0638%, corresponding to a relative reduction of approximately 42.9%, while the recovery time decreases from 0.0288 s to 0.0080 s, corresponding to a relative reduction of approximately 72.2%.

These results demonstrate that the principal performance advantage of the proposed MFDC lies in its rapid rejection of sudden load-torque variations, particularly under medium- and high-speed operating conditions. Compared with the speed-step results in Fig. 7, the load-step results in Fig. 9 provide more consistent evidence of the disturbance-rejection capability of the second-order ultra-local model and the online lumped-disturbance compensation mechanism.

A comparison of dynamic response performances between the two methods under all load-step operating conditions is summarized in Table 4.

6. CONCLUSION

To address problems of limited speed-loop bandwidth in the conventional cascaded speed control of SMPMSM for electric vehicles and the poor robustness of model-based control methods, this study proposes a model-free direct speed control method based on a second-order ultra-local model. The main research conclusions are summarized as follows:

1. A second-order speed ultra-local model was established to directly relate the mechanical speed of the SMPMSM to the q-axis reference voltage. This formulation removes the explicit q-axis current loop from the speed-control channel and avoids the bandwidth separation imposed by the conventional cascaded speed-current architecture.
2. A model-free direct speed controller and a virtual q-axis current ultra-local-model-based torque-limiting strategy were developed. The lumped effects of parameter uncertainties, inverter nonlinearities, load-torque variations, and unmodeled dynamics are estimated from sampled input-output data. The proposed voltage-limiting strategy constrains the q-axis current and electromagnetic torque

without introducing an additional load-torque observer or reconstructing a cascaded q-axis current-control loop.

3. Experimental results demonstrate that the proposed MFDC provides its clearest performance advantages under medium- and high-speed load-disturbance conditions. At 500 r/min, the load-step speed fluctuation is reduced from 3.6152% to 2.0638%, and the recovery time is shortened from 0.0288 s to 0.0080 s. Under rated-speed step conditions, the speed overshoot is reduced from 2.8028% to 2.2136%, and the recovery time is shortened from 0.2128 s to 0.1949 s. However, the proposed method does not outperform the conventional MFC under every low-speed speed-step condition, indicating that further improvement in low-speed speed estimation and disturbance-estimator design is required.
4. The experimental validation was limited to a 48-V laboratory-scale SMPMSM drive platform rated at 13 N·m and 500 r/min. Thus, the current results establish the feasibility of the proposed control framework on the available prototype but cannot be directly generalized to high-voltage and high-power traction-grade systems. Although the basic ultra-local modeling framework is not inherently tied to a specific voltage or power rating, practical traction applications may involve more severe voltage saturation, current constraints, inverter nonlinearities, switching-frequency limitations, sensing and computation delays, thermal parameter variations, and field-weakening requirements. Future work will validate the proposed method on higher-power drive platforms, investigate its operation over wider speed and torque ranges, and evaluate its long-term robustness with thermal and parameter variations.

ACKNOWLEDGEMENT

The study was supported by grant the National Natural Science Foundation of China (Grant No. W2023JSKF0252) from the Foundation of Basic Research. This work was carried out under research program the Fundamental Research Funds for the Central Universities (Program No. W2023JSKF0252) of Hefei University of Technology.

REFERENCES

[1] Mao, H. S., "Review on the development status and sales forecasting methods of new energy vehicles," *China Economic & Trade Herald*, No. 4, 88–90, 2025.

[2] Cai, S., J. L. Kirtley, and C. H. T. Lee, "Critical review of direct-drive electrical machine systems for electric and hybrid electric vehicles," *IEEE Transactions on Energy Conversion*, Vol. 37, No. 4, 2657–2668, Dec. 2022.

[3] Li, T., X. Sun, G. Lei, Y. Guo, Z. Yang, and J. Zhu, "Finite-control-set model predictive control of permanent magnet synchronous motor drive systems — an overview," *IEEE/CAA Journal of Automatica Sinica*, Vol. 9, No. 12, 2087–2105, Dec. 2022.

[4] Kong, D., H. Cai, and W. Zeng, "A predefined time fast terminal sliding mode predictive speed control for PMSM drives," *IEEE Transactions on Power Electronics*, Vol. 40, No. 7, 9068–9079, Jul. 2025.

[5] Wang, L., H. Zhu, and Z. Yang, "Tuning method for PI controllers of PMSM driving system," *Transactions of China Electrotechnical Society*, Vol. 29, No. 5, 104–117, 2014.

[6] Zhao, M., Y. Cao, C. Li, Z. Wang, T. Shi, and C. Xia, "Expanded limit boundary explicit model predictive direct speed control for PMSMs," *IEEE Transactions on Power Electronics*, Vol. 39, No. 5, 6089–6101, May 2024.

[7] Song, W., J. Li, C. Ma, Y. Xia, and B. Yu, "A simple tuning method of PI regulators in FOC for PMSM drives based on deadbeat predictive conception," *IEEE Transactions on Transportation Electrification*, Vol. 10, No. 4, 9852–9863, Dec. 2024.

[8] Tian, M., T. Wang, Y. Yu, Q. Dong, B. Wang, and D. Xu, "Integrated observer-based terminal sliding-mode speed controller for PMSM drives considering multisource disturbances," *IEEE Transactions on Power Electronics*, Vol. 39, No. 7, 7968–7979, Jul. 2024.

[9] Liu, Z., X. Huang, Q. Hu, G. Yang, Y. Wang, and J. Shen, "Model-free predictive current control of PMSM using modified extended state observer," *IEEE Transactions on Power Electronics*, Vol. 40, No. 1, 679–690, Jan. 2025.

[10] Shi, T., S. Lin, Y. Cao, and Y. Yan, "A two-degree-of-freedom explicit model predictive noncascaded direct speed control for SPMSM drives," *IEEE Transactions on Transportation Electrification*, Vol. 11, No. 1, 510–520, Feb. 2025.

[11] Sun, X., T. Li, M. Yao, G. Lei, Y. Guo, and J. Zhu, "Improved finite-control-set model predictive control with virtual vectors for PMSHM drives," *IEEE Transactions on Energy Conversion*, Vol. 37, No. 3, 1885–1894, Sep. 2022.

[12] Zhou, Y., H. Li, R. Liu, and J. Mao, "Continuous voltage vector model-free predictive current control of surface mounted permanent magnet synchronous motor," *IEEE Transactions on Energy Conversion*, Vol. 34, No. 2, 899–908, Jun. 2019.

[13] Gao, X., M. Abdelrahem, C. M. Hackl, Z. Zhang, and R. Kennel, "Direct predictive speed control with a sliding manifold term for PMSM drives," *IEEE Journal of Emerging and Selected Topics in Power Electronics*, Vol. 8, No. 2, 1258–1267, Jun. 2020.

[14] Liu, M., J. Hu, K. W. Chan, S. W. Or, S. L. Ho, W. Xu, and X. Zhang, "Dual cost function model predictive direct speed control with duty ratio optimization for PMSM drives," *IEEE Access*, Vol. 8, 126 637–126 647, 2020.

[15] Kawai, H., Z. Zhang, R. Kennel, and S. Doki, "Direct speed control based on finite control set model predictive control with voltage smoother," *IEEE Transactions on Industrial Electronics*, Vol. 70, No. 3, 2363–2372, Mar. 2023.

[16] Zhang, Y., C. Liu, S. Li, K. Cao, Y. Yang, and Z. Cheng, "No weighting factor pmsm model predictive torque control based on composite sliding mode disturbance observer." *Progress In Electromagnetics Research B*, Vol. 113, 63–76, 2025.

[17] Gong, Z., C. Zhang, X. Ba, and Y. Guo, "Improved deadbeat predictive current control of permanent magnet synchronous motor using a novel stator current and disturbance observer," *IEEE Access*, Vol. 9, 142 815–142 826, 2021.

[18] Liu, J., S. Vazquez, L. Wu, A. Marquez, H. Gao, and L. G. Franquelo, "Extended state observer-based sliding-mode control for three-phase power converters," *IEEE Transactions on Industrial Electronics*, Vol. 64, No. 1, 22–31, Jan. 2017.

[19] Fliess, M. and C. Join, "Model-free control," *International Journal of Control*, Vol. 86, No. 12, 2228–2252, 2013.

[20] Yang, L., H. Li, J. Huang, Z. Zhang, and H. Zhao, "Model predictive direct speed control with novel cost function for SMPMSM drives," *IEEE Transactions on Power Electronics*, Vol. 37, No. 8, 9586–9595, Aug. 2022.

[21] Mao, J., H. Li, L. Yang, X. Wang, and R. Liu, "Adaptive integral-type direct speed control of SMPMSM drive system based on ultra-local model," *IEEJ Transactions on Electrical and Electronic Engineering*, Vol. 17, No. 4, 592–600, 2022.

[22] Han, J., "From PID to active disturbance rejection control," *IEEE Transactions on Industrial Electronics*, Vol. 56, No. 3, 900–906, Mar. 2009.

[23] Ma, Y. and Y. Li, "Active disturbance compensation based robust control for speed regulation system of permanent magnet synchronous motor," *Applied Sciences*, Vol. 10, No. 2, 709, 2020.

[24] Wu, H., C. Gan, H. Wang, S. Wang, R. Qu, and X. Liu, "Active disturbance rejection speed control with double-stage-ESO considering aperiodic and periodic disturbances for PMSM drives," *IEEE Transactions on Industrial Electronics*, 2025.

[25] Wen, D., W. Zhang, Z. Tang, X. Zhang, and Z. Cheng, "Model predictive control with ESO and an improved speed loop for PMSM," *Progress In Electromagnetics Research C*, Vol. 142, 107–117, 2024.

[26] Huang, Y., Y. Xie, W. Han, and L. Ling, "Parameter-adaptive composite active disturbance rejection control for permanent magnet synchronous motor drives," *Progress In Electromagnetics Research B*, Vol. 114, 13–25, 2025.

[27] Fliess, M. and C. Join, "An alternative to proportional-integral and proportional-integral-derivative regulators: Intelligent proportional-derivative regulators," *International Journal of Robust and Nonlinear Control*, Vol. 32, No. 18, 9512–9524, 2022.